Intrinsic Optical Spatial Differentiation Enabled Quantum Dark-Field Microscopy

Jiawei Liu, Qiang Yang, Shizhen Chen, Zhicheng Xiao, Shuangchun Wen, and Hailu Luo*
Laboratory for Spin Photonics, School of Physics and Electronics, Hunan University, Changsha 410082, China

(Received 24 November 2021; accepted 13 April 2022; published 13 May 2022)

By solving the Maxwell's equations in Fourier space, we find that the cross-polarized component of the dipole scattering field can be written as the second-order spatial differentiation of the copolarized component. This differential operation can be regarded as intrinsic which naturally arises as consequence of the transversality of electromagnetic fields. By introducing the intrinsic spatial differentiation into heralded single-photon microscopy imaging technique, it makes the structure of pure-phase object clearly visible at low photon level, avoiding any biophysical damages to living cells. Based on the polarization entanglement, the switch between dark-field imaging and bright-field imaging is remotely controlled in the heralding arm. This research enriches both fields of optical analog computing and quantum microscopy, opening a promising route toward a nondestructive imaging of living biological systems.

DOI: 10.1103/PhysRevLett.128.193601

Quantum microscopy is an important tool to characterize the microstructure and understand the dynamics of a living system with quantum-correlated illumination [1–5]. The sensitivity and resolution of the conventionally used microscopy are fundamentally limited by environmental noise, which arises from the system-environment interaction. The effects of environmental noise can be effectively reduced by increasing the intensity of the illumination light. For photosensitive biological samples, however, the biophysical damage typically arises due to the large illumination intensities [6,7]. It has been known that quantum correlations can be used to extract more information for per photon used in an optical precise measurements [8,9]. Recently, the importance of improving sensitivity has motivated efforts to apply quantum-correlated photons in optical microscopy [10,11]. For some biological specimens, the thickness and refractive index inhomogeneity determine how much light scattering it produces. This class of specimens is referred to as phase objects, as they affect significantly only the phase of the input field rather than the amplitude [12]. Too little scattering from the specimen makes it challenging to reveal the structure from an overwhelming input light background [13,14].

In this Letter, we report a quantum dark-field microscopy by introducing the optical spatial differentiation into the quantum-correlated imaging technique. This differential operation can be regarded as intrinsic which naturally arises as a consequence of the transversality of electromagnetic fields. For pure-phase objects, differential operations can reveal the edge features of objects, since the phase gradient generally occurs at the edge. In the Fourier space, it can be understood as blocking the low wave vectors, such that only scattered light related to high wave vectors can reach the detector [15]. Our quantum dark-field microscopy scheme has several distinguishing features. (1) The intrinsic differential operation makes the structure of the pure-phase object clearly visible at a low photon level, and thus avoiding any biophysical damages. (2) The switch between bright-field and dark-field microscopy is remotely controlled in the heralding arm, without changing anything on the imaging arm. (3) The signal photons are detected only within a short time window when heralded photons trigger, which prevents almost all environmental noise photons from detection, and therefore achieving quantum microscopy images with a high contrast.

In standard electromagnetic theory, the Hertz vector potential provides an intuitive physical picture of electromagnetic field emitted by an oscillating dipole [16,17]. The electric field $\tilde{\mathbf{E}}(\mathbf{k},t)$ and the magnetic field $\tilde{\mathbf{B}}(\mathbf{k},t)$ of dipole scattering are determined by Maxwell's equations which can be written in the Fourier space: $i\mathbf{k}\cdot\tilde{\mathbf{E}}(\mathbf{k},t)=0$, $i\mathbf{k}\cdot\tilde{\mathbf{B}}(\mathbf{k},t)=0$, $i\mathbf{k}\times\tilde{\mathbf{E}}(\mathbf{k},t)+\partial\tilde{\mathbf{B}}(\mathbf{k},t)/\partial t=0$, and $i\mathbf{k}\times\tilde{\mathbf{B}}(\mathbf{k},t)-1/c^2\partial\tilde{\mathbf{E}}(\mathbf{k},t)/\partial t=0$, where c is the speed of light in vacuum. Under external field illumination, the phase object can be considered to be composed of oscillating electric dipoles (Fig. 1). To satisfy the transversality of electromagnetic field, the Hertz vector potential $\tilde{\mathbf{\Pi}}(\mathbf{k},t)$ is introduced to describe the scattering fields:

$$\tilde{\mathbf{E}}(\mathbf{k},t)=-\mathbf{k}\times[\mathbf{k}\times\tilde{\mathbf{\Pi}}(\mathbf{k},t)]. \tag{1}$$

Here, $\tilde{\mathbf{\Pi}}(\mathbf{k},t)=\mathbf{f}\tilde{\phi}(\mathbf{k},t)/k^2$ can be written as the product of a constant unit vector and a scalar potential [18,19]. The vector $\mathbf{f}=f_x\mathbf{e}_x+f_y\mathbf{e}_y$ is determined by the input state of polarization, and the scalar potential $\tilde{\phi}(\mathbf{k},t)$ is the Fourier transformation of $\phi(\mathbf{r},t)$. The Hertz vector potential requires $\phi(\mathbf{r},t)$ to satisfy the Helmholtz wave equation:

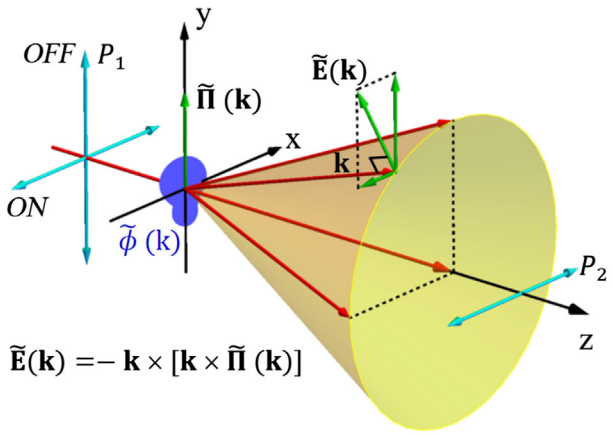

FIG. 1. The electromagnetic field emitted by an oscillating dipole. The Hertz vector potential $\tilde{\mathbf{\Pi}}(\mathbf{k})$ is introduced to describe the scattering field $\tilde{\mathbf{E}}(\mathbf{k})$. The scalar potential $\tilde{\phi}(\mathbf{k})$ is determined by the structure of phase object. Different output field components are obtained by switching the polarizations states (*on* or *off*).

$$\nabla^2\phi(\mathbf{r},t) - \frac{1}{c^2}\frac{\partial^2\phi(\mathbf{r},t)}{\partial t^2} = 0. \tag{2}$$

We introduce two polarizers (P_1 and P_2) to analyze the dipole scattering field as shown in Fig. 1. Consider an input state of polarization with $\mathbf{f} = f_y\mathbf{e}_y$, then from Eq. (1), the electric field of dipole scattering can be obtained as

$$\tilde{\mathbf{E}}(k_x,k_y) = \frac{1}{k^2}[k_xk_y\mathbf{e}_x + (k^2 - k_y{}^2)\mathbf{e}_y + k_yk_z\mathbf{e}_z]\tilde{\phi}(k_x,k_y). \tag{3}$$

Here, $\tilde{\phi}(k_x,k_y)$ is determined by the phase structure of the object. When the two polarizers are parallel (orthogonal) to each other, the copolarized (cross-polarized) component in the output port is obtained. In the microscopy imaging system, the copolarized component can be regarded as the bright field $\tilde{E}_{\text{bright}}(k_x,k_y)$, and the cross-polarized component can serve as the dark field $\tilde{E}_{\text{dark}}(k_x,k_y)$. From Eq. (3) we get

$$\tilde{E}_{\text{dark}}(k_x,k_y) \propto k_xk_y\tilde{E}_{\text{bright}}(k_x,k_y). \tag{4}$$

The transfer function between the bright- and dark-field is expressed as $H(k_x,k_y) \propto k_xk_y$ [see Supplemental Material (SM), Sec. I [20]]. Here, the two crossed polarizers work as a high k pass filter, i.e., high k vectors pass through the system, while the low k vectors are blocked in the Fourier space. After the inverse Fourier transform, Eq. (4) can be written as

$$E_{\text{dark}}(x,y) \propto \frac{\partial^2 E_{\text{bright}}(x,y)}{\partial x\partial y}. \tag{5}$$

Therefore, the dark-field image can be achieved by a second-order differential operation of the bright-field image.

For a pure-phase object with phase distribution $\varphi(x,y)$, the output field only experiences a phase change. The output bright field can be obtained as $E_{\text{bright}}(x,y) = \exp[i\varphi(x,y)]$, which shows no contrast in the bright-field image due to

$$I_{\text{bright}}(x,y) = |\exp[i\varphi(x,y)]|^2 = 1. \tag{6}$$

After the differential operation, the output dark field is obtained as $E_{\text{dark}}(x,y) = \partial^2\exp[i\varphi(x,y)]/\partial x\partial y$, and the intensity can be written as

$$I_{\text{dark}}(x,y) = \left|\frac{\partial^2\exp[i\varphi(x,y)]}{\partial x\partial y}\right|^2. \tag{7}$$

The edge-enhanced images will be obtained, since the phase gradient generally occurs at the edge of the phase object (see SM, Sec. II [20]). Note that nanostructured devices have been extrinsically introduced to perform the differential operations on optical fields, and to enhance the edges of features in optical phase images [22–27]. Here, the optical differential operations can be regarded as the intrinsic properties of the Maxwell's equations, without involving any precise fabrication of nanostructures.

The expected performance of the switchable quantum dark-field imaging scheme is illustrated in Fig. 2(a). There are two optical arms in the microscopy imaging system: one is imaging arm and the other is heralding one. The cell specimen is illuminated by polarized photons in the imaging arm. For $|H\rangle$ input photons, almost all of photons will pass through the polarizer along horizontal direction, resulting in a bright-field image. For $|V\rangle$ input photons, a few $|H\rangle$ photons are generated during the processing of dipole scattering. The $|H\rangle$ photons associated with high k will pass through the polarizer, resulting in a dark-field image [Fig. 2(b)]. The image should be a quantum superposition of a bright-field image and a dark-field image without knowing the polarization states of heralding photons. The polarization entangled photons with the state of $(1/\sqrt{2})(|HH\rangle + |VV\rangle)$ are used as an illumination source to implement the switchable quantum microscopy images. When the state of input photons in the heralding arm is set to $|H\rangle$ or $|V\rangle$, thus the state of input photons in the imaging arm will also be $|H\rangle$ or $|V\rangle$. This is why the imaging mode can be remotely controlled by the heralding arm.

A schematic diagram of the quantum dark-field microscope is shown in Fig. 3(a). The polarization entangled photon source consists of a pump laser and a Sagnac interferometer. The pump source is a single-frequency diode laser at 405 nm. The pump beam is focused by a pair of lenses to get a beam waist (40 μm) at the center of a 20 mm long type-II phase matched PPKTP crystal. The pump power between clockwise and counterclockwise

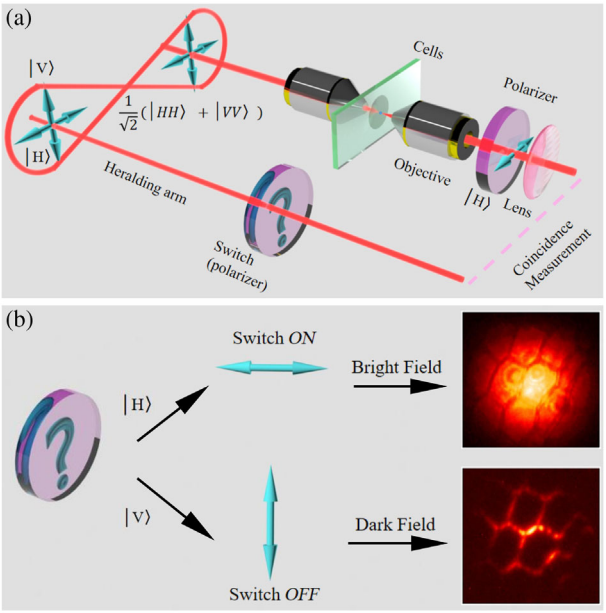

FIG. 2. The schematic of switchable quantum bright- and dark-field imaging. (a) In the imaging arm, biological cells are centered between two microscope objectives. The polarization of entangled photon pairs is $(1/\sqrt{2})(|HH\rangle + |VV\rangle)$, the question mark in the heralding arm means polarization selection of idler photons is unknown. The dashed line stands for the electrical path. (b) The switch state *on* or *off* of the heralding arm. When the idler photons of the heralding arm are projected to $|H\rangle$, it indicates the switch in the *on* state and leads to a bright-field image. While the heralded photons are projected to $|V\rangle$, a dark-field image is obtained with the switch in the *off* state.

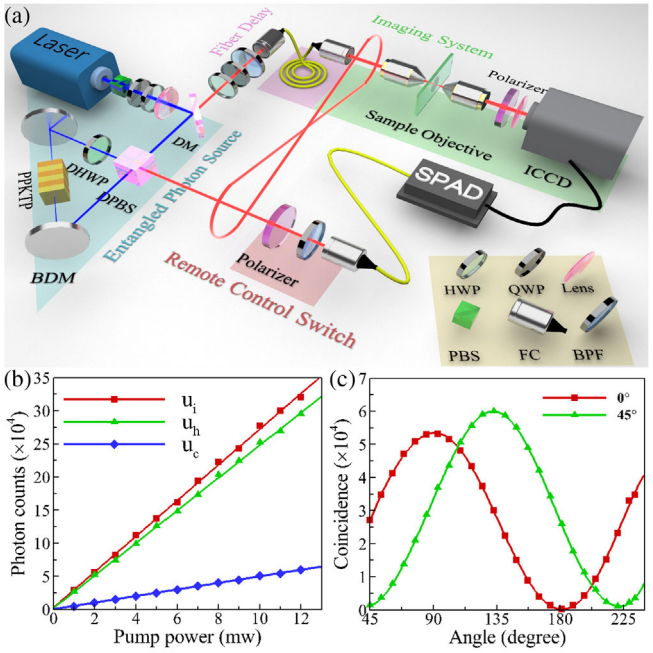

FIG. 3. Experimental setup of quantum dark-field microscope. (a) Setup schematic. BDM, broadband dielectric mirror; PPKTP crystal, periodically poled $KTiOPO_4$ crystal; DPBS, dual-wavelength polarization beam splitter; PBS, polarization beam splitter; DM, dichromatic mirror; FC, fiber coupler; BPF, band-pass filter; DHWP, dual-wavelength half wave plate; HWP, half wave plate; QWP, quarter wave plate; SPAD, single photon avalanche detector; ICCD, intensified charge coupled device. The blue (red) light path presents the 405 nm (810 nm) light. The bright-field microscope system is constructed by two confocal microscope objectives ($10\times$, NA $= 0.25$). (b) Photon counts of signal side (u_i), heralding side (u_h), and coincidence (u_c) under different pump powers. (c) Coincidence counts as a function of the polarized angle.

directions in Sagnac loop is kept balanced by the combination of a quarter wave plate (QWP) and a half wave plate (HWP). The Sagnac interferometer consists of a dual-wavelength polarization beam splitter (DPBS), two broadband dielectric mirrors and a dual-wavelength HWP (DHWP). The DHWP is fixed at 45° to obtain the horizontal polarization of the counterclockwise pump directions in front of the crystal. The down-converted photon pairs pumped by two counterpropagating beams are separated by DPBS. They are collimated by two fiber couplers. In our case, the polarization entangled state $|\Phi\rangle = (1/\sqrt{2})(|HH\rangle + |VV\rangle)$ is employed by adjusting the combination of HWP and QWP in front of the imaging arm [28–30].

To characterize the quality of the generated polarization entangled state, two-photon coincidence counts and polarization interference are performed. In the coincidence counts, we replace the dark-field imaging system with a SPAD. The photon counts of single side and coincidence under different pump powers are measured in the Fig. 3(b). It is shown that the coincidence photons increase linearly as the pump power (see SM, Sec. III [20]). To measure the polarization interference fringes, a polarizer is added in the imaging arm whose polarized axis is fixed at 0° or 45° [28]. The measured results of quantum interferences are shown in Fig. 3(c). By calculating $Z = (C_{\max} - C_{\min})/(C_{\max} + C_{\min})$, the visibilities of interference fringe are $96.6 \pm 0.1\%$ in the $+45°/-45°$ basis and $98.9 \pm 0.1\%$ in the H/V basis, respectively. The visibilities exceed 71%, the bound required to violate the Bell's inequality [31,32]. Therefore, the polarization entangled photon source meets the requirement of microscopy imaging applications.

We acquire images using two different system configurations: direct imaging and heralded imaging. In the direct imaging scheme, the ICCD is internally triggered, and both the signal photons and environmental noise photons will be continuously accumulated. The signal-to-noise ratio (SNR) is then given by [33]

$$R_D = \frac{N_i t}{\sqrt{N_i t + (N_b + N_d)t}}, \tag{8}$$

where N_i is the number of counts due to signal photons, t is the integration time, N_b is counts arising from

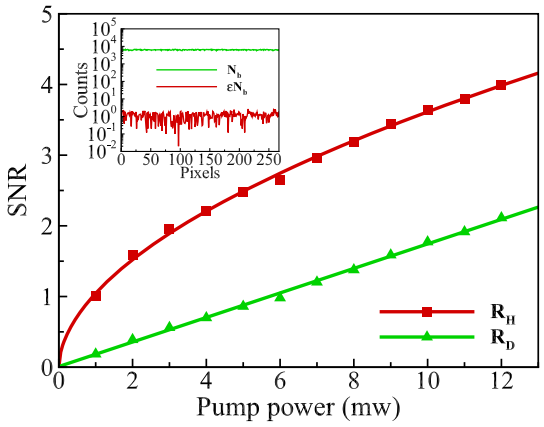

FIG. 4. Experimental results of SNR in direct imaging and heralded imaging under different pump powers. The inset shows the photon counts of environmental noise detected in direct imaging and heralded imaging with pump power 12 mW. The fraction of the noise photons falling within the gate time is estimated as $\varepsilon = 0.0002$.

environmental noise, and N_d is the detector dark counts. The units of N_i, N_b, and N_d are per second per pixel. At low photon flux, the signal photon level is comparable to (or even smaller than) environmental photon noise, which will result in an image with very low SNR. For the heralded imaging scheme, the ICCD is externally triggered, and the SNR is modified as

$$R_H = \frac{hN_i t}{\sqrt{hN_i t + \varepsilon(N_b + N_d)t}}, \tag{9}$$

where $h = u_c/\sqrt{u_i u_h}$ is the correlation ratio and ε is the fraction of the noise photons falling within the gate time. The signal photons are accumulated in the ICCD only within a short time window (4 ns), which prevents almost all noise photons from detection, and therefore achieve a high SNR (Fig. 4) (see SM, Sec. IV [20]). The SNR is expected to be further enhanced by reducing the shot noise [34,35].

Figures 5(a) and 5(b) show direct bright-field image and direct dark-field image, where the ICCD is internally triggered. As a comparison, the corresponding images that are externally triggered by the heralding detector are shown in Figs. 5(c) and 5(d). All images are acquired by the ICCD with 100 s integration times (see SM, Sec. III [20]). The cross-section intensity distributions along the dashed lines in Figs. 5(a)–5(d) are shown in Figs. 5(e)–5(h), respectively. The stem-parenchyma cell is regarded as a pure-phase object, it is invisible in the bright-field imaging, however, it can be observed in the dark-field imaging. To evaluate the advantage of the quantum protocol of dark-field microscopy, we calculate the image contrast which can be defined as [6]

$$V_{D/H} = \frac{I_{\max} - I_{\min}}{I_{\max} + I_{\min}}. \tag{10}$$

When using the direct imaging method, the contrast of dark-field image is $V_D \approx 0.093$ as shown in Fig. 5(f). For the external trigger imaging, equivalent experimental conditions are used, including low photon level and integration time. The quantum heralded imaging method provides

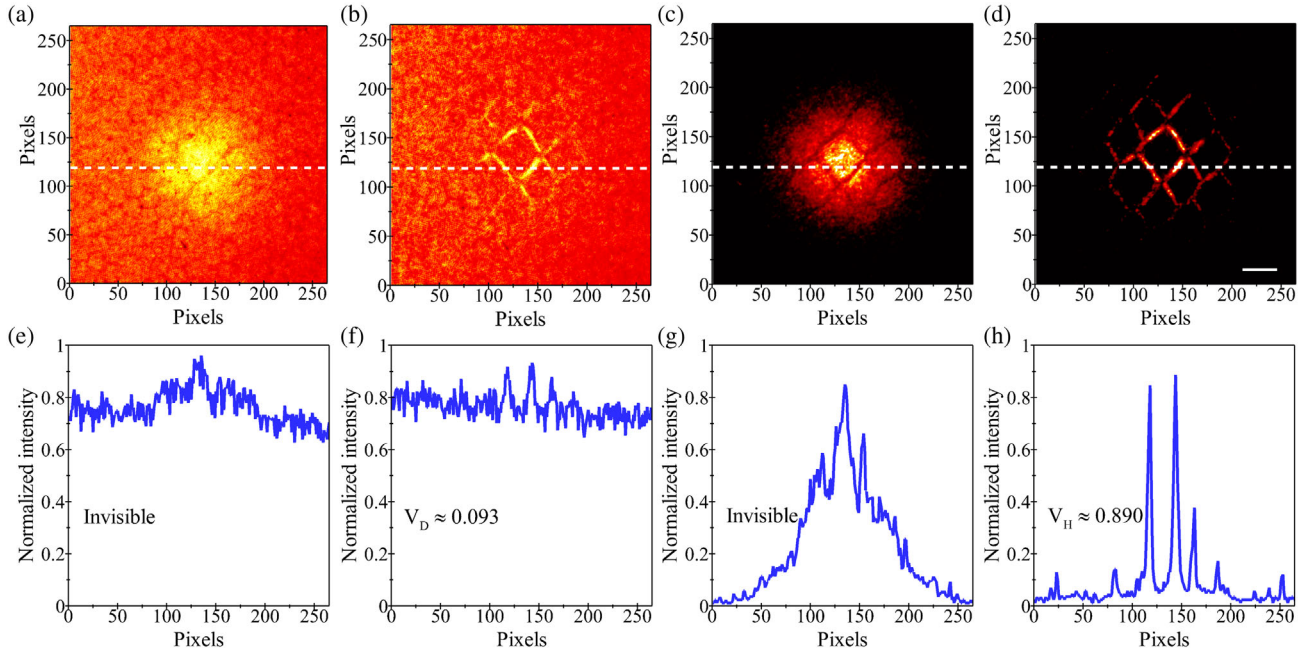

FIG. 5. Quantum enabled microscopy images of stem-parenchyma cells. (a) and (b) Direct bright-field image and direct dark-field image where the ICCD is internally triggered. (c) and (d) The bright-field image and dark-field image are triggered by the heralding detector. (e)–(h) are taken along the white dashed lines in (a)–(d), respectively. Scale bar, 30 μm.

$V_H \approx 0.890$ as shown in Fig. 5(h), corresponding to an enhancement of $V_H/V_D \approx 9.570$.

Our nonlocal imaging is fundamentally different from previous quantum imaging techniques, such as ghost imaging [36–39] or interaction-free imaging [40]. The pure-phase ghost image may be realized by an appropriate choice of the spatial filter in the ghost imaging system [41]. Alternatively, differential ghost imaging [42] and phase-shifting interferometry [43] have been employed to obtain the information of the phase object. The proposed intrinsic differential scheme may be applied to realize the pure-phase ghost image. Our results also demonstrate the previous findings that the quantum heralded imaging would achieve a higher contrast at a low photon level [44]. However, there is no advantage for the heralded imaging scheme when using large signal illumination (see SM, Sec. V [20]).

In conclusion, we have proposed and demonstrated a quantum dark-field microscopy scheme which makes the structure of pure-phase objects clearly visible at the low photon level. The dark-field image can be achieved by performing two-dimensional differential operations on the optical field, and to enhance the edge features of phase objects. We have found that the optical spatial differentiation naturally arises in the dipole scattering field by solving the Maxwell's equations in Fourier space. Based on the polarization entanglement, the switch between dark-field imaging and bright-field imaging is remotely controlled in the heralding arm. In our system, the signal photons are detected in the ICCD only within a short time window, which prevents almost all environmental noise photons from detection, and therefore achieve quantum microscopy images with a high contrast. The combination of the optical spatial differentiation and the heralded single-photon imaging technique enabled quantum dark-field microscopy, opens an important pathway toward a nondestructive imaging of living biological system.

This work was supported by the National Natural Science Foundation of China (Grants No. 12174097 and No. 61835004).

*hailuluo@hnu.edu.cn

[1] F. Wolfgramm, C. Vitelli, F. A. Beduini, N. Godbout, and M. W. Mitchell, Entanglement-enhanced probing of a delicate material system, Nat. Photonics **7**, 28 (2013).

[2] Y. Israel, S. Rosen, and Y. Silberberg, Supersensitive Polarization Microscopy Using NOON States of Light, Phys. Rev. Lett. **112**, 103604 (2014).

[3] M. A. Taylor, J. Janousek, V. Daria, J. Knittel, B. Hage, H.-A. Bachor, and W. P. Bowen, Subdiffraction-Limited Quantum Imaging within a Living Cell, Phys. Rev. X **4**, 011017 (2014).

[4] M. A. Taylor and W. P. Bowen, Quantum metrology and its application in biology, Phys. Rep. **615**, 1 (2016).

[5] P. A. Moreau, E. Toninelli, T. Gregory, and M. J. Padgett, Imaging with quantum states of light, Nat. Rev. Phys. **1**, 367 (2019).

[6] P. A. Morris, R. S. Aspden, J. E. C. Bell, R. W. Boyd, and M. J. Padgett, Imaging with a small number of photons, Nat. Commun. **6**, 5913 (2015).

[7] C. A. Casacio, L. S. Madsen, A. Terrasson, M. Waleed, K. Barnscheidt, B. Hage, M. A. Taylor, and W. P. Bowen, Quantum-enhanced nonlinear microscopy, Nature (London) **594**, 201 (2021).

[8] M. Napolitano, M. Koschorreck, B. Dubost, N. Behbood, R. J. Sewell, and M. W. Mitchell, Interaction-based quantum metrology showing scaling beyond the Heisenberg limit, Nature (London) **471**, 486 (2011).

[9] G. Chen, L. Zhang, W.-H. Zhang, X.-X. Peng, L. Xu, Z.-D. Liu, X.-Y. Xu, J.-S. Tang, Y.-N. Sun, D.-Y. He, J.-S. Xu, Z.-Q. Zhou, C.-F. Li, and G.-C. Guo, Achieving Heisenberg-Scaling Precision with Projective Measurement on Single Photons, Phys. Rev. Lett. **121**, 060506 (2018).

[10] T. Ono, R. Okamoto, and S. Takeuchi, An entanglement-enhanced microscope, Nat. Commun. **4**, 2426 (2013).

[11] R. Tenne, U. Rossman, B. Rephael, Y. Israel, A. K. Ptaszek, R. Lapkiewicz, Y. Silberberg, and D. Oron, Super-resolution enhancement by quantum image scanning microscopy, Nat. Photonics **13**, 116 (2019).

[12] F. Zernike, How I discovered phase contrast, Science **121**, 345 (1955).

[13] Y. Park, C. Depeursinge, and G. Popescu, Quantitative phase imaging in biomedicine, Nat. Photonics **12**, 578 (2018).

[14] H. Kwon, E. Arbabi, S. M. Kamali, M. Faraji-Dana, and A. Faraon, Single-shot quantitative phase gradient microscopy using a system of multifunctional metasurfaces, Nat. Photonics **14**, 109 (2020).

[15] C. A. C. Chazot, S. Nagelberg, C. J. Rowlands, M. R. J. Scherer, I. Coropceanu, K. Broderick, Y. Kim, M. G. Bawendi, P. T. C. So, and M. Kolle, Luminescent surfaces with tailored angular emission for compact dark-field imaging devices, Nat. Photonics **14**, 310 (2020).

[16] J. A. Stratton, *Electromagnetic Theory* (John Wiley and Sons, New York, 1941).

[17] J. D. Jackson, *Classical Electrodynamics* (Wiley, New York, 1999).

[18] A. Aiello and M. Ornigotti, Near field of an oscillating electric dipole and cross-polarization of a collimated beam of light: Two sides of the same coin, Am. J. Phys. **82**, 860 (2014).

[19] M. Ornigotti and A. Aiello, The Hertz vector revisited: A simple physical picture, J. Opt. **16**, 105705 (2014).

[20] See Supplemental Material at http://link.aps.org/supplemental/10.1103/PhysRevLett.128.193601 for information about the derivation of the field in the dipole scattering, the optical spatial differentiation of pure-phase objects, the details of experimental measurements, the experimental measurements of SNR, and two-photon coincidence imaging with classically correlated pulses, which includes Ref. [21].

[21] K. Guo, E. N. Christensen, J. B. Christensen, J. G. Koefoed, D. Bacco, Y. Ding, H. Ou, and K. Rottwitt, High coincidence-to-accidental ratio continuous-wave photon pair generation in a grating-coupled silicon strip waveguide, Appl. Phys. Express **10**, 062801 (2017).

[22] T. Zhu, Y. Zhou, Y. Lou, H. Ye, M. Qiu, Z. Ruan, and S. Fan, Plasmonic computing of spatial differentiation, Nat. Commun. **8**, 15391 (2017).
[23] H. Kwon, D. Sounas, A. Cordaro, A. Polman, and A. Alù, Nonlocal Metasurfaces for Optical Signal Processing, Phys. Rev. Lett. **121**, 173004 (2018).
[24] J. Zhou, H. Qian, C. F. Chen, J. Zhao, G. Li, Q. Wu, H. Luo, S. Wen, and Z. Liu, Optical edge detection based on high-efficiency dielectric metasurface, Proc. Natl. Acad. Sci. U.S.A. **116**, 11137 (2019).
[25] Y. Zhou, H. Zheng, I. I. Kravchenko, and J. Valentine, Flat optics for image differentiation, Nat. Photonics **14**, 316 (2020).
[26] L. Wesemann, J. Rickett, J. Song, J. Lou, E. Hinde, T. J. Davis, and A. Roberts, Nanophotonics enhanced coverslip for phase imaging in biology, Light Sci. Appl. **10**, 98 (2021).
[27] J. Zhou, H. Qian, J. Zhao, M. Tang, Q. Wu, M. Lei, H. Luo, S. Wen, and Z. Liu, Two-dimensional optical spatial differentiation and high-contrast imaging, Natl. Sci. Rev. **8**, nwaa176 (2021).
[28] T. Kim, M. Fiorentino, and F. N. C. Wong, Phase-stable source of polarization-entangled photons using a polarization Sagnac interferometer, Phys. Rev. A **73**, 012316 (2006).
[29] B. Fickler, M. Krenn, R. Lapkiewicz, S. Ramelow, and A. Zeilinger, Real-time imaging of quantum entanglement, Sci. Rep. **3**, 1914 (2013).
[30] J. Zhou, S. Liu, H. Qian, Y. Li, H. Luo, S. Wen, Z. Zhou, G. Guo, B. Shi, and Z. Liu, Metasurface enabled quantum edge detection, Sci. Adv. **6**, eabc4385 (2020).
[31] J. F. Clauser and A. Shimony, Bell's theorem. Experimental tests and implications, Rep. Prog. Phys. **41**, 1881 (1978).
[32] R. Horodecki, P. Horodecki, M. Horodecki, and K. Horodecki, Quantum entanglement, Rev. Mod. Phys. **81**, 865 (2009).
[33] S. Johnson, A. McMillan, C. Torre, S. Frick, J. Parity, and M. Padgett, Single-pixel imaging with heralded single photons, Opt. Continuum. **1**, 826 (2022).
[34] G. Brida, M. Genovese, and I. R. Berchera, Experimental realization of sub-shot-noise quantum imaging, Nat. Photonics **4**, 227 (2010).
[35] N. Samantaray, I. Ruo-Berchera, A. Meda, and M. Genovese, Realization of the first sub-shot-noise wide field microscope, Light Sci. Appl. **6**, e17005 (2017).
[36] J. H. Shapiro and R. W. Boyd, The physics of ghost imaging, Quantum Inf. Process. **11**, 949 (2012).
[37] R. S. Bennink, S. J. Bentley, and R. W. Boyd, "Two-Photon" Coincidence Imaging with a Classical Source, Phys. Rev. Lett. **89**, 113601 (2002).
[38] A. F. Abouraddy, P. R. Stone, A. V. Sergienko, B. E. A. Saleh, and M. C. Teich, Entangled-photon Imaging of a Pure Phase Object, Phys. Rev. Lett. **93**, 213903 (2004).
[39] J. H. Shapiro, Computational ghost imaging, Phys. Rev. A **78**, 061802(R) (2008).
[40] G. B. Lemos, V. Borish, G. D. Cole, S. Ramelow, R. Lapkiewicz, and A. Zeilinger, Quantum imaging with undetected photons, Nature (London) **512**, 409 (2014).
[41] T. Shirai, T. Setälä, and A. T. Friberg, Ghost imaging of phase objects with classical incoherent light, Phys. Rev. A **84**, 041801(R) (2011).
[42] F. Ferri, D. Magatti, L. A. Lugiato, and A. Gatti, Differential Ghost Imaging, Phys. Rev. Lett. **104**, 253603 (2010).
[43] R. Borghi, F. Gori, and M. Santarsiero, Phase and Amplitude Retrieval in Ghost Diffraction from Field-Correlation Measurements, Phys. Rev. Lett. **96**, 183901 (2006).
[44] D. G. England, B. Balaji, and B. J. Sussman, Quantum-enhanced standoff detection using correlated photon pairs, Phys. Rev. A **99**, 023828 (2019).